Inter-filament resistance, effective transverse resistivity and coupling loss in superconducting multi-filamentary NbTi and Nb_3Sn strands

2012 Supercond. Sci. Technol. 25 065018

(http://iopscience.iop.org/0953-2048/25/6/065018)

Supercond. Sci. Technol. **25** (2012) 065018 (9pp) doi:10.1088/0953-2048/25/6/065018

Inter-filament resistance, effective transverse resistivity and coupling loss in superconducting multi-filamentary NbTi and Nb_3Sn strands

C Zhou, Y Miyoshi, E P A van Lanen, M Dhallé and A Nijhuis

Energy, Materials and Systems, Faculty of Science and Technology, University of Twente, 7522ND Enschede, The Netherlands

E-mail: c.zhou@utwente.nl

Received 23 December 2011, in final form 21 March 2012
Published 27 April 2012
Online at stacks.iop.org/SUST/25/065018

Abstract

The effective transverse resistivity of a range of multi-filamentary Nb_3Sn and NbTi strands is measured with a direct four-probe method and the data are compared to the transverse resistivity values obtained from AC coupling loss experiments. Correspondence between both is satisfactory provided that all contributions to the current path are properly taken into account.

Quantitative knowledge of the inter-filament resistance and of the effective transverse strand resistivity leads to a better insight into the physical mechanisms that govern not only AC coupling losses, but also a variety of current distribution and redistribution processes, e.g. the current entry length in short-sample measurements or critical current degradation with bending strain.

The wires are state-of-the-art commercial superconductors that are presently applied in ITER, JT-60SA and LHC magnets. The influence of filament-to-matrix contact resistance, of the (possibly inhomogeneous) matrix resistivity and of the cross-sectional strand layout on the AC coupling losses in these wires is discussed.

(Some figures may appear in colour only in the online journal)

1. Introduction

In practical multi-filamentary superconductors, twisted filaments are embedded in a normal metal matrix for AC loss reduction, for stabilization against local disturbances and for protection against quenches [1, 2]. The inter-filament resistance is an essential parameter whenever a detailed and quantitative description of intra-strand current redistribution processes is needed [2, 3], e.g. to describe the V–I characteristics and the critical current degradation with a strain and/or crack distribution generated by electromagnetic and mechanical loads in stressed strain-sensitive Nb_3Sn filaments [4–7]. The effective transverse resistivity, on the other hand, is a parameter that combines the matrix resistivity, the filament-to-matrix contact resistance and the internal strand structure [8], and determines the level of coupling losses in AC regimes [2, 9].

A number of techniques that measure the effective transverse resistivity indirectly are well established: self-field diffusion [10–12]; intra-strand coupling losses at low frequency [9, 13, 14]; and current transfer lengths in short-sample measurements [15, 16]. However, for a precise description of the current distribution among filaments and the matrix, direct four-probe experiments to measure the inter-filament resistance have been developed [17] and recently expanded [17, 18]. Compared to the effective transverse resistivity, these experiments provide additional information which can be used e.g. to optimize the strand

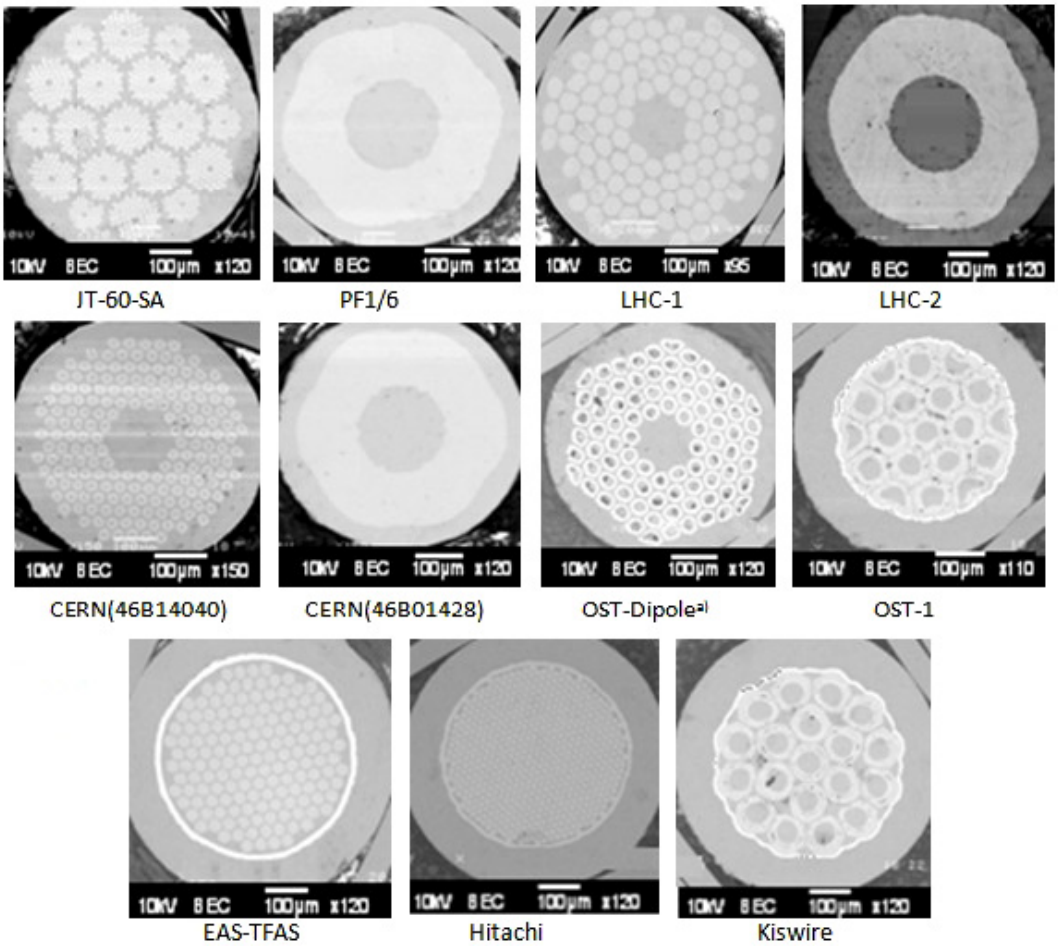

Figure 1. Cross-sectional photos of the investigated strands.

layout and composition for AC loss minimization or for reduced stress sensitivity.

Note that the direct methods yield resistance values R (expressed in Ω), whereas the indirect experiments yield resistivity values ρ (in Ω m). To compare both, one needs to take the geometrical layout of the strand properly into account. In this paper, we first express the inter-filament resistance data R_{4p} obtained with direct four-probe experiments in terms of both the effective transverse resistivity $\rho_{tf,4p}$ of the filamentary zone and the effective transverse resistivity $\rho_{t0,4p}$ of the strand as a whole. (A symbol list describing various resistive and geometrical parameters is given in appendix A.) These resistivity values are then compared with equivalent data obtained from indirect experiments: the filamentary transverse resistivity $\rho_{tf,D}$ measured with self-field diffusion and the overall transverse resistivity $\rho_{t0,AC}$ measured with AC coupling loss. Data are obtained on six NbTi and five Nb_3Sn strands, which are all state-of-the-art superconductors that are applied in ITER, JT-60SA or LHC magnets.

The paper is arranged as follows. Section 2 gives the main strand characteristics, briefly describes the four-probe and AC loss experiments, and presents the data obtained with these measurements. Section 3.1 (and appendices B and C) shows how the transverse resistivity ρ_{tf} of the filamentary zone can be derived from the matrix resistivity ρ_m and from the filament-to-matrix contact resistance $R_\square$, and then compares the obtained $\rho_{tf,4p}$ values with equivalent literature data from self-field diffusion experiments. In section 3.2 (and appendix D) we add the possible contributions of stabilizing cores, sheaths and/or barriers to obtain the overall transverse resistivity $\rho_{t0,4p}$ of the strands. These values are compared with the equivalent data from our AC loss measurements.

2. Experimental details and results

2.1. Strand characteristics

SEM micrographs of all the investigated strands are shown in figure 1, while their key characteristics are given in table 1. The tested NbTi and Nb_3Sn strands were selected to have a wide variation in terms of filament number and diameter; of matrix materials (Cu, CuMn, bronze); and of cross-sectional layout (with or without matrix core, outer sheath and diffusion barrier).

Table 1. Strand characteristics.

Sample	Number of filaments	Diameter of strand (mm)	Diameter of filaments (μm)	Twist pitch L_p (mm)	Matrix
JT-60-SA (candidate) NbTi	1 189	0.81	16	16	Cu
PF 1/6 NbTi	4 488	0.73	6.5	15	Cu
LHC-1 NbTi	8 800	1.065	7	18	Cu
LHC-2 NbTi	6 425	0.825	6	15	Cu
CERN(46B14040) NbTi	14 040	0.6	2.6	10	Cu/CuMn
CERN(46B01428) NbTi	8 900	0.6	4	6	Cu
OST-dipole[a] Nb_3Sn(RRP)[b]	8 712	0.81	3	15	Cu
OST-1 Nb_3Sn(IT)[c]	2 869	0.82	6	15	Bronze
EAS-TFAS Nb_3Sn(BR)[d]	8 305	0.81	3	17	Bronze
Hitachi Nb_3Sn(BR)	11 077	0.828	3.2	15	Bronze
Kiswire Nb_3Sn(IT)	3 419	0.84	6	15	Bronze

[a] OST is Oxford Superconducting Technology; the OST Nb_3Sn strand, used for the EDIPO dipole coil, presently under construction, has 84 bundles with 104 fine filaments per bundle that are interlinked by sintering.

[b] RRP: restacked-rod-process route.

[c] IT: internal-tin route.

[d] BR: bronze route.

Table 2. Global and local matrix resistivity, filament-to-matrix contact resistance and effective transverse strand resistivity of the investigated samples.

Samples	Matrix	ρ_m (RRR, Ω m) ($\times 10^{-10}$)	ρ_{mf} (EDX, Ω m) ($\times 10^{-8}$)	$R_\square$ (Ω m^2) ($\times 10^{-15}$)	$\rho_{t0,AC}$ (Ω m) ($\times 10^{-10}$)
JT-60-SA (candidate)	Cu	0.8		4.0	1.4
PF 1/6	Cu	1.2		5.5	3.1
LHC-1	Cu	1.6		7.5	2.7
LHC-2	Cu	1.1		5.5	3.1
CERN (46B14040)	Cu/CuMn	1.8		5.5	4.6
CERN (46B01428)	Cu	2.1		5.5	6.3
OST-dipole	Cu	0.7	17	10	2.8
OST-1	Bronze	1.1	11	3.0	10
EAS-TFAS	Bronze	1.8	1.3	1.0	12
Hitachi	Bronze	1.2	2.8	1.0	76
Kiswire	Bronze	1.8	13	3.0	65

2.2. Four-probe measurement of intra-strand resistances

The four-probe direct measurements are described in more detail elsewhere [18, 19]. Essentially, thin cross-sectional slices (around 20–30 μm) of the strands are prepared with a double polishing technique. These samples are cooled below the critical temperature T_c on a cold finger and with the aid of micro-manipulators four tungsten needles are positioned anywhere on the cross-section, serving as current and voltage probes for a series of intra-strand resistance measurements R_{4p}.

To extract the filament-to-matrix contact resistance $R_\square$ from these R_{4p} values, two-dimensional FEM (COMSOL) models of the strands are used. The models incorporate the strand layout as well as the overall and local matrix resistivities ρ_m and ρ_{mf}. The latter quantities are estimated from independent RRR measurements and from EDX characterization of the local Sn content [20, 21] and are shown in table 2. The only remaining free variable in the models is then the filament-to-matrix contact resistance $R_\square$. This parameter is solved for the given strand geometry and measured parameters to get the best possible correspondence with the measured R_{4p} data, and its values are included in table 2. As discussed in sections 3.1 and 3.2, the matrix resistivities ρ_m and ρ_{mf}, together with the contact resistance $R_\square$, provide the fundamental contributions to the effective transverse resistivities ρ_{tf} and $\rho_{t0,4p}$.

2.3. AC coupling loss measurements

Strand coupling losses in a perpendicular field were separated from hysteresis loss in the usual way, by assuming that hysteresis loss at low excitation is independent of the field sweep rate [6, 9, 22]. AC losses in ~2 m long coiled strands were measured in $B = \pm 3$ T field cycles with different sweep rates, ranging from 5 to 200 mT s^{-1}. The magnetometer used is equipped with superconducting pick-up coils, which offers high accuracy at low ramp rates [23, 24]. The data can be used directly to derive the experimental average transverse

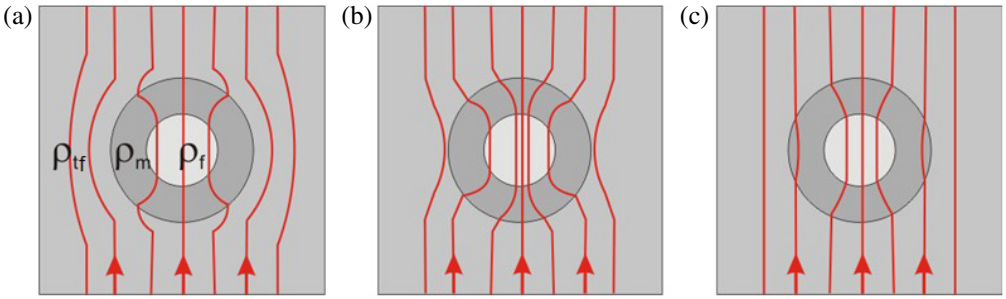

Figure 2. Transverse current flow around a composite cylinder embedded in a homogeneous medium with (a) relatively lower or (b) relatively higher resistivity. For a specific value of the medium resistivity (c), the current flow pattern outside the cylinder will be undisturbed.

resistivity $\rho_{t0,AC}$, which is given by:

$$\rho_{t0,AC} = \frac{2\Delta B}{\alpha}\left(\frac{L_p}{2\pi}\right)^2, \quad (1)$$

where L_p is the filament twist pitch and α is the slope of the loss plotted against frequency [6]. The derived values are included in table 2.

2.4. Experimental results

With the experimental measurements and simulation models, the values of filament-to-matrix contact resistivity $R_\square$ and experimental effective transverse resistivity $\rho_{t0,AC}$ of the various strands are extracted and listed in table 2 [19].

All the values of the filament-to-matrix contact resistivity $R_\square$ are in the range 10^{-15}–10^{-14} Ω m^2, clustered around 5–6$\times 10^{-15}$ Ω m^2 for the NbTi strands. As shown below, these parameters give a better insight into the transverse current flow pattern and allow for a quantitative description of current redistribution processes inside strands.

3. Comparison with indirect methods

In order to validate the extracted intra-strand resistivities from direct measurements with indirect measurements, the strand effective transverse resistivity is crucial, as it is the physical parameter governing AC coupling loss of superconducting strands. Combining the extracted filament-to-matrix contact resistivity, matrix resistivity (RRR and simulation) and geometry of cross-section, the overall strand average transverse resistivity can be determined, thus calculating the coupling loss so as to crosscheck it with the AC coupling loss measurement. The derivations of effective filament resistivity and effective transverse resistivity in the filamentary zone, a detailed analysis of coupling loss in composite wires, and comparisons between calculation and measurement are presented step by step in this section.

3.1. Effective filament resistivity

First of all, with the aim of deriving the average transverse resistivity, as well as a more distinct picture of the current distribution and pattern inside a strand, the effective filament resistivity is defined and calculated. To be more specific, we replace the zero-resistance filaments surrounded by a resistive contact layer with $R_\square$ (expressed in Ω m^2) by resistive filaments with an effective filament resistivity ρ_f (expressed in Ω m). The effective filament resistivity was analytically solved, and also crosschecked with COMSOL (FEM) simulations constructed according with real strand cases [19]; its formula is shown in appendix B.

3.2. Effective transverse resistivity in the filamentary zone

Based on effective filament resistivity, we take one further step towards the effective transverse resistivity in the filament zone involving the matrix resistivity around the filaments. The central idea behind this derivation is the same as that used in asymmetric effective medium theory, as proposed by Carr [25, 26]. Consider a cylinder consisting of a core with resistivity ρ_f (the effective filament resistivity discussed above) and a coaxial mantle with resistivity ρ_m (the resistivity of the metal matrix). This composite cylinder is embedded in a homogeneous material with resistivity ρ_{tf}. ρ_{tf} will be the effective 'replacement' resistivity for an ensemble of composite cylinders consisting of a filamentary core and a metal mantle, the so-called effective transverse resistivity in the filamentary zone. This specific value is the effective transverse resistivity of the filament/matrix composite, which leaves the current outside the composite cylinder being neither repelled (figure 2(a), inputting with a relatively lower resistivity value) nor attracted (figure 2(b), inputting with a relatively higher resistivity value), but remaining undisturbed (figure 2(c), inputting with the right proper resistivity value) by the inner composite cylinder.

The formulas are presented in appendix C, and the results for the effective filament resistivity and transverse resistivity in the filamentary zone are listed in table 3. As indicated in table 3, in the investigated strands, the effective filament resistivity is higher than the matrix resistivity in all the NbTi and OST-dipole strands, but lower in other Nb_3Sn strands. The former matrix is copper, while the latter one is bronze; their resistivities are listed in table 2. That, together with the formulas in appendix C, also explain the much higher effective transverse resistivity in the filament zone in Nb_3Sn than in NbTi strands.

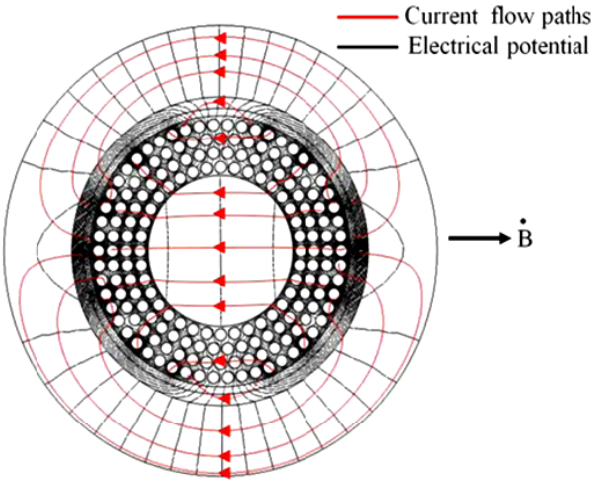

Figure 3. Schematic pattern of coupling current flow and electrical potential in the transverse cross-section of a multi-filament composite wire under an external AC field.

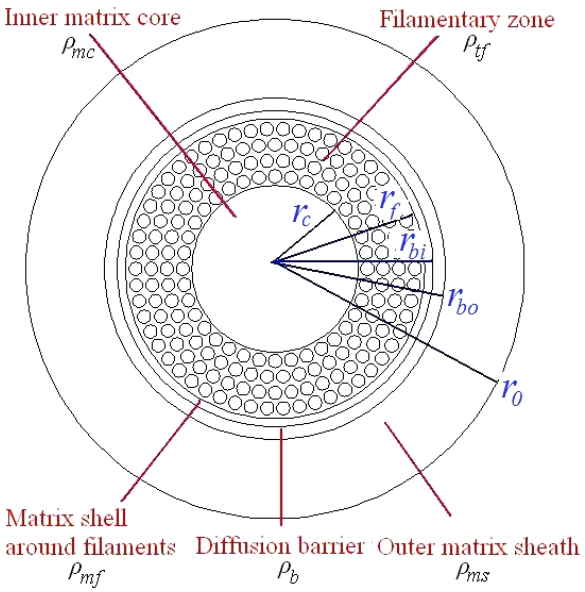

Figure 4. Cross-section and composite distribution of a multi-filament strand.

Table 3. Calculation results of effective filament resistivity and transverse resistivity in the filamentary zone.

Samples	ρ_f (Ω m) ($\times 10^{-10}$)	ρ_{tf} (Ω m) ($\times 10^{-10}$)
JT-60	4.3	1.5
PF 1/6	17	3.6
LHC-1	22	3.4
LHC-2	18	3.9
CERN (46B14040)	42	6.0
CERN (46B01428)	27	5.3
OST-dipole	29	3.2
OST-1	10	480
EAS-TFAS	6.7	170
Hitachi	6.3	61
Kiswire	10	430

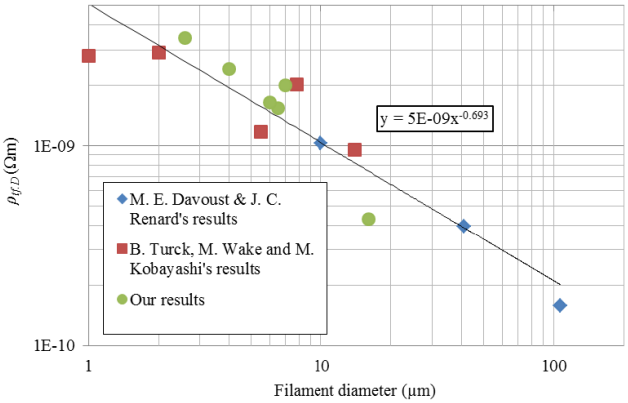

Figure 5. Average transverse resistivity around filaments versus filament diameter.

3.3. Calculation of coupling loss

After finding the effective transverse resistivity in the filamentary zone, the strand coupling loss can be quantitatively calculated, providing a bridge between the basic parameters of the strand and the AC coupling loss. As shown in figure 3, coupling currents flow across the matrix in the inner core, filamentary region as well as in the outer sheath, and return as super currents through the filaments, which creates an additional homogeneous field exactly in the opposite direction to the external field. This electric field provides detailed information on the transposition achieved in a given composite [9]. Calculations for coupling loss power in a composite wire (see figure 4) are presented in appendix D.

3.4. Comparison of effective transverse resistivity around a filament with diffusion measurements

The first validation is made for $R_{\square}$ and ρ_{mf} in the filamentary zone. Turck has investigated the transverse resistance between filaments by measuring the decay of the pinned currents after a full cycle in various NbTi wires, which is also called the diffusion phenomenon [10, 27]. The main parameter determining the diffusion process is the magnetic diffusivity of the composite, which can be extracted by experimental measurement. With measurements and calculations, the transverse resistivity $\rho_{tf,D}$ can be estimated from $R_{\square}$ and ρ_{mf} (see appendix E).

The comparison shows a good agreement with previous results given by Davoust and Renard [28] and measurement results by Turck [10] (see figure 5), and validates the extracted intra-strand resistivities (especially $R_{\square}$ and ρ_{mf}) from direct measurements.

3.5. Coupling loss in outer matrix sheath

The coupling loss in the outer matrix sheath is obtained by AC magnetization measurements in three strands, with

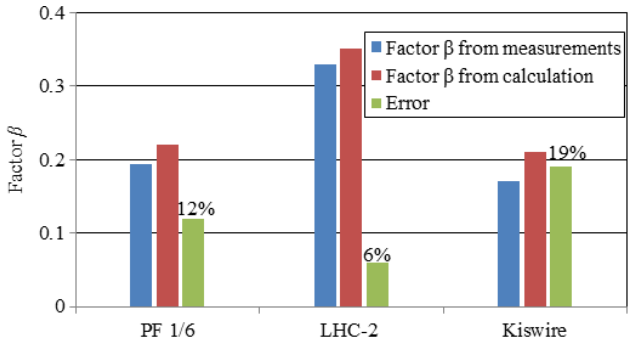

Figure 6. The percentage of coupling loss in the outer matrix sheath of PF 1/6, LHC-2 and Kiswire strands.

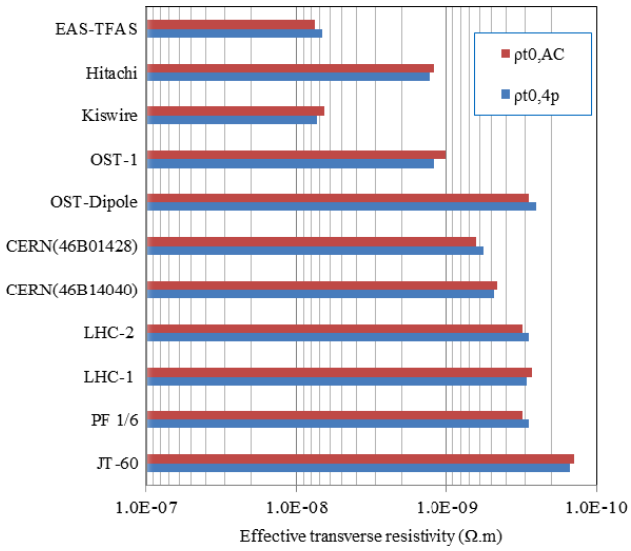

Figure 7. Experimental and calculated results of total effective transverse resistivity ρ_{t_0} in various wires.

and without an outer matrix sheath, so as to verify both extracted intra-strand resistivities and coupling loss calculations. As indicated in figure 6, the low resistive matrix outer sheath carries relatively high coupling current flows, generating 20% to 30% of the coupling loss. Moreover, the percentage of coupling loss in the matrix outer shell (factor β, see appendix F) shows a good match between calculations and experimental measurements. The error is around 10%, except for the Kiswire strand, which has an extremely low coupling loss leading to a low accuracy in the magnetization measurements. The comparison provides not only further positive support to the extracted intra-strand resistivities, but also the impact of the outer matrix sheath on coupling loss.

3.6. Comparison with measured AC losses

Finally, with the above correlations ascertained, the average transverse resistivity can be crosschecked between $\rho_{t0,AC}$

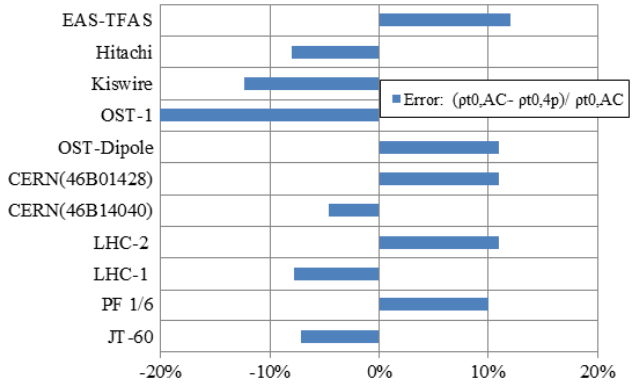

Figure 8. Comparison of experimental and calculated results of ρ_{t_0} in various wires.

from measurement and $\rho_{t0,4p}$ from calculation. Detailed calculations are described in appendices D and G respectively, comparisons for all investigated strands are presented in figures 7 and 8. According to the comparison shown in figure 8, a good agreement is achieved, with errors mostly less than 12%. Moreover, Nb_3Sn strands show higher errors than NbTi strands due to the lower accuracy in the coupling loss measurements, especially OST-1 (20%) and Kiswire (13%) with very similar internal-tin cross-sections, in which it is also difficult to distinguish the filament zone and inner core. Nevertheless, a valid and reasonable way was found to estimate the average effective transverse resistivity and coupling loss with the basic strand parameters, which gives a solid basis for optimizing the strand design and manufacture, as well as predicting the strand performance together with a detailed multi-filamentary strand model, as presented in [29].

4. Conclusion

Based on a wide range of multi-filament NbTi and Nb_3Sn strands, direct and indirect experimental measurements and calculations on filament-to-matrix contact resistance, matrix resistivity, effective transverse resistivity in the filamentary zone and the overall strand, coupling loss, as well as the interactions among all of them have been presented and analyzed. All the values of the filament-to-matrix contact resistivity $R_\square$ are in the range 10^{-15}–10^{-14} Ω m^2, clustered around 5–6 $\times$ 10^{-15} Ω m^2 for the NbTi strands.

The extracted characteristic parameters and combined theoretical calculations show a solid basis for predicting the coupling loss with basic strand parameters. The extracted results on the intra-strand resistivity parameters provide a good understanding of the mechanisms governing the intra-strand current distribution. The available data will be further used for exploration of correlations between strand performance under varying strain conditions and strand architecture.

Appendix A. Symbol list

Parameter	Unit	Description	Experiment/ formula
R_{4p}	Ω	Inter-filament resistance	Four-probe
ρ_m	Ω m	Overall longitudinal matrix resistivity	RRR
ρ_{mf}	Ω m	Matrix resistivity filamentary zone	EDX
$R_\square$	Ω m^2	Filament-to-matrix contact resistance	Four-probe + FEM
ρ_f	Ω m	Effective filament resistivity	Calculation from appendix B
ρ_b	Ω m	Diffusion barrier resistivity	Material property
ρ_{tf}	Ω m	Transverse resistivity filamentary zone	Calculation from appendix C
ρ_{ms}	Ω m	Matrix resistivity outer sheath	RRR
ρ_{mc}	Ω m	Matrix resistivity inner core	RRR
$\rho_{t0,4p}$	Ω m	Overall transverse resistivity strand (directly comparable to $r_{t0,AC}$)	Calculation from appendix D
$\rho_{t0,AC}$	Ω m	Overall transverse resistivity strand (directly comparable to $r_{t0,4p}$)	AC coupling loss
ρ_{fb}	Ω m	Barrier resistivity around filament	Appendix E
$\rho_{tf,D}$	Ω m	Transverse resistivity filamentary zone (directly comparable to diffusion measurement)	Current diffusion appendix E
β	—	Percentage of coupling loss in matrix outer shell	AC coupling loss measurement and calculation
P	w	Total coupling loss power	Coupling loss calculation
r_0	m	Strand radius	Microscopy
r_f	m	Filament radius	Microscopy
λ	—	Superconducting fill factor filamentary zone	
L_p	m	Twist pitch	
b	m	Barrier thickness	Microscopy
w	m	Filament spacing	Microscopy
r_c	m	Inner core radius	Microscopy
r_{bi}	m	Inner barrier radius	Microscopy
r_{bo}	m	Outer barrier radius	Microscopy

Appendix B. Effective filament resistivity

$$\rho_f = \frac{R_\square}{r_f}. \tag{B.1}$$

The effective filament resistivity ρ_f is simply the contact resistance $R_\square$ divided by the filament radius r_f.

Appendix C. Effective transverse resistivity in filamentary zone

To find ρ_{tf}, the electric potential distribution in the composite cylinder needs to be worked out by solving the two-dimensional Laplace equation in cylindrical coordinates [25], applying the appropriate boundary conditions. As a result, the relation between ρ_m, ρ_f and ρ_{tf} is:

$$\frac{\rho_{tf}}{\rho_m} = \frac{(1-\lambda)\rho_m + (1+\lambda)\rho_f}{(1+\lambda)\rho_m + (1-\lambda)\rho_f} \tag{C.1}$$

which is the expression for the effective transverse resistivity in the filamentary zone that we sought. λ, equal to $(r_f/r_m)^2$, is the superconducting-filament/normal matrix ratio in the filament zone.

For a 3-layer case, there is a diffusion barrier around the filament between the filament and the matrix, with resistivity ρ_b and thickness d. The relation between ρ_m, ρ_f, ρ_b and ρ_{tf} is:

$$\frac{\rho_{tf}}{\rho_m} = \frac{(1-\lambda')\rho'_m + (1+\lambda')\rho'_b}{(1+\lambda')\rho'_m + (1-\lambda')\rho'_b}, \tag{C.2}$$

where

$$\begin{aligned} \rho'_b &= \rho_b[r_b^2(\rho_f+\rho_b) + r_f^2(\rho_f-\rho_b)], \\ \rho'_m &= \rho_m[r_b^2(\rho_f+\rho_b) - r_f^2(\rho_f-\rho_b)], \\ \lambda' &= \lambda\frac{r_b^2}{r_m^2} \\ r_b &= r_f + d. \end{aligned} \tag{C.3}$$

Appendix D. Overall transverse resistivity and coupling loss

The following formula derivations in this section are based on the analysis and calculations of coupling loss power in a multi-filament composite from Turck [30, 31].

As indicated in figure 4, the total coupling loss power in a wire with only an outer matrix sheath and filamentary zone is:

$$P_{01} = \left(\frac{r_f}{r_0}\right)^2 \dot{B}^2 \left(\frac{L_p}{2\pi}\right)^2 \left(\frac{1}{\rho_{ms}}\frac{r_0^2 - r_f^2}{r_0^2 + r_f^2} + \frac{1}{\rho_{tf}}\right) + \frac{\dot{B}^2}{4\rho_{ms}}\left(\frac{r_0^4 - r_f^4}{r_0^2}\right). \tag{D.1}$$

The total coupling loss power in a wire with an outer matrix sheath, filamentary zone and inner matrix core is:

$$P_{02} = \left(\frac{r_f}{r_0}\right)^2 \dot{B}^2 \left(\frac{L_p}{2\pi}\right)^2 \left(\frac{1}{\rho_{ms}}\frac{r_0^2 - r_f^2}{r_0^2 + r_f^2} + \frac{1}{\rho_{tf}}\frac{r_f^2 - r_c^2}{r_f^2} + \frac{1}{\rho_{mc}}\frac{r_c^2}{r_f^2}\right) + \frac{\dot{B}^2}{4\rho_{ms}}\left(\frac{r_0^4 - r_f^4}{r_0^2}\right). \tag{D.2}$$

The total coupling loss power in the above wire after etching the outer matrix sheath is:

$$P'_{02} = \dot{B}^2 \left(\frac{L_p}{2\pi}\right)^2 \left(\frac{1}{\rho_{tf}}\frac{r_f^2 - r_c^2}{r_f^2} + \frac{1}{\rho_{mc}}\frac{r_c^2}{r_f^2}\right). \tag{D.3}$$

The total coupling loss power in a wire with an outer matrix sheath, diffusion barrier, matrix layer around filamentary zone and filamentary zone is:

$$P_{03} = \left(\frac{r_f}{r_0}\right)^2 \dot{B}^2 \left(\frac{L_p}{2\pi}\right)^2 \left(\frac{q}{\rho_{ms}} + \frac{n}{\rho_b} + \frac{m}{\rho_{mf}} + \frac{1}{\rho_{tf}}\right) + \frac{\dot{B}^2}{4\rho_{ms}}\left(\frac{r_0^4 - r_{bo}^4}{r_0^2}\right), \tag{D.4}$$

where

$$\begin{aligned} m &= \frac{r_{bi}^2 - r_f^2}{r_f^2}(r_f^2 + \delta^2 r_{bi}^2)a_1^2, \\ n &= \frac{r_{bo}^2 - r_{bi}^2}{R_{bi}^2}(r_{bi}^2 + \gamma^2 r_{bo}^2)a_2^2, \\ q &= \frac{r_0^2 - r_{bo}^2}{r_{bo}^2}(r_{bo}^2 + r_0^2)a_3^2, \quad a_1 = \frac{r_f}{r_f^2 + \delta r_{bi}^2}, \\ a_2 &= \frac{a_1(1+\delta)r_{bi}^2}{r_{bi}^2 + \gamma r_{bo}^2}, \qquad a_3 = \frac{a_2(1+\gamma)r_{bo}^2}{r_{bo}^2 + r_0^2}, \\ \gamma &= \frac{\rho_{ms}(r_0^2 + r_{bo}^2) + \rho_b(r_0^2 - r_{bo}^2)}{\rho_{ms}(r_0^2 + r_{bo}^2) - \rho_b(r_0^2 - r_{bo}^2)}, \\ \delta &= \frac{\rho_b(r_{bi}^2 + \gamma r_{bo}^2) + \rho_{mf}(\gamma r_{bo}^2 - r_{bi}^2)}{\rho_b(r_{bi}^2 + \gamma r_{bo}^2) - \rho_{mf}(\gamma r_{bo}^2 - r_{bi}^2)}. \end{aligned} \tag{D.5}$$

The total coupling loss power in the above wire after etching the outer matrix sheath is [32]:

$$P'_{03} = \left(\frac{r_f}{r_{bo}}\right)^2 \dot{B}^2 \left(\frac{L_p}{2\pi}\right)^2 \left(\frac{n}{\rho_b} + \frac{m}{\rho_{mf}} + \frac{1}{\rho_{tf}}\right) + \frac{\dot{B}^2}{4\rho_b}\left(\frac{r_{bo}^4 - r_{bi}^4}{r_{bo}^2}\right), \tag{D.6}$$

where

$$\begin{aligned} m &= \frac{r_{bi}^2 - r_f^2}{R_f^2}(r_f^2 + S r_{bi}^2)a_1^2, \\ n &= \frac{r_{bo}^2 - r_{bi}^2}{r_b^2}(r_{bi}^2 + r_{bo}^2)a_2^2, \\ a_1 &= \frac{r_f}{r_f^2 + S r_{bi}^2} \qquad a_2 = \frac{a_1(1+S)r_{bi}^2}{r_{bi}^2 + r_{bo}^2}, \\ S &= \frac{\rho_b(r_{bo}^2 + r_{bi}^2) + \rho_{mf}(r_{bo}^2 - r_{bi}^2)}{\rho_b(r_{bo}^2 + r_{bi}^2) - \rho_{mf}(r_{bo}^2 - r_{bi}^2)}. \end{aligned} \tag{D.7}$$

Above all, eddy current losses in the inner matrix core can be neglected compared to the coupling losses.

Appendix E. Effective transverse resistivity around the filament

The $\rho_{tf,D}$ in [10] is the average transverse resistivity in the filamentary zone. To make a correlation with our work, we first define the resistivity of the thin barrier around the filament ρ_{fb} [10] from $R_\square$ and barrier thickness b. With the assumption that the thickness of this barrier is orders of magnitude smaller than the filament diameter, we can derive ρ_{fb} as:

$$\rho_{fb} = \frac{R_\square}{b}. \tag{E.1}$$

Combined with the extracted matrix resistivity in the filamentary zone ρ_{mf}, the geometry parameters (filament diameter, d; matrix spacing among filaments, w), and formula equation (16) in [10] we can determine $\rho_{tf,D}$:

$$\rho_{tf,D} = \rho_{fb}\frac{2b}{d + 2b + w} + \rho_{mf}\frac{w}{d + 2b + w}. \tag{E.2}$$

Appendix F. Coupling losses in the outer matrix sheath

Here, the factor β represents the fraction of coupling loss in the matrix outer shell.

$$\beta = \frac{P_0 V_0 - P'_0 V'_0}{P_0 V_0}, \tag{F.1}$$

where P_0 is coupling loss power determined from the equation in appendix D and V_0 is the volume of the strand.

Appendix G. Average transverse resistivity

The total average transverse resistivity $\rho_{t0,4p}$ is determined by the equation:

$$\rho_{t0,4p} = \frac{\dot{B}^2}{P_0}\left(\frac{L_p}{2\pi}\right)^2, \tag{G.1}$$

where P_0 is the coupling loss power determined from the equation in appendix D corresponding to different strand cross-sectional layouts.

References

[1] Takács S 1997 *Supercond. Sci. Technol.* **10** 733–48
[2] Wilson M N 1983 *Superconducting Magnets* (Oxford: Oxford University Press)
[3] Ekin J W 1978 *J. Appl. Phys.* **49** 3406–9
[4] Nijhuis A *et al* 2005 *Supercond. Sci. Technol.* **18** S273–83
[5] Nunoya Y, Isono T and Okuno K 2004 *IEEE Trans. Appl. Supercond.* **14** 1468–72
[6] Nijhuis A, Ilyin Y and Abbas W 2008 *Supercond. Sci. Technol.* **12** 065001
[7] Muzzi L, Corato V, Viola R and della Corte A 2008 *J. Appl. Phys.* **103** 073915
[8] Goldfarb B and Itoh K 1994 *J. Appl. Phys.* **75** 2115–8
[9] G Ries 1977 *IEEE Trans. Magn.* **13** 524–6
[10] Turck B, Wake M and Kobayashi M 1977 *Cryogenics* **17** 217–23
[11] Ishibashi K *et al* 1979 *Cryogenics* **19** 161–6
[12] Duchateau J L, Turck B, Krempasky L and Polak M 1976 *Cryogenics* **16** 97–102
[13] Nijhuis A, Ilyin Y, Abbas W and Wessel W A J 2007 *IEEE Trans. Appl. Supercond.* **17** 2680–3
[14] Carr W J 1983 *AC Loss and Macroscopic Theory of Superconductors* (London: Gordon and Breach)
[15] Holúbek T, Dhallé M and Kovác P 2007 *Supercond. Sci. Technol.* **20** 123–8
[16] Stenvall A, Korpela A, Lehtonen J and Mikkonen R 2007 *Supercond. Sci. Technol.* **20** 92–9

[17] Corato V, Muzzi L, Besi Vetrella U and della Corte A 2009 *J. Appl. Phys.* **105** 093930
[18] Zhou C, van Lanen E P A, Veldhuis D, ten Kate H H J, Dhallé M and Nijhuis A 2011 *IEEE Trans. Appl. Supercond.* **21** 2501–4
[19] Zhou C, Miyoshi Y, van Lanen E P A, Dhallé M and Nijhuis A 2012 *Supercond. Sci. Technol.* **25** 015013
[20] Fickett F R 1982 *Cryogenics* **22** 135–8
[21] Simon N J, Drexler E S and Reed R P 1992 (*NIST Monograph* vol 177) (Boulder, CO: NIST) pp 850–1
[22] Campbell A M 1982 *Cryogenics* **22** 3–16
[23] Verweij A P, Eriksson L E and ten Kate H H J 1993 *Supercollider* **5** 587–90
[24] Verweij A P 1995 Electrodynamics of superconducting cables in accelerator magnets *PhD Thesis* University of Twente
[25] Moon P and Spencer D E 1971 *Field Theory Handbook* (Berlin: Springer)
[26] Carr W J 1974 *J Appl. Phys.* **45** 929–35
[27] Ishibashi K, Wake M, Kobayashi M and Katase A 1979 *Cryogenics* **19** 161–6
[28] Davoust M E and Renard J C 1976 *Proc. ICEC 6* (London: IPC Science and Technology) pp 458–69
[29] Miyoshi Y, Zhou C, van Lanen E P A, Dhallé M M J and Nijhuis A 2012 Modelling of current distribution in Nb_3Sn multifilamentary strands subjected to bending *Supercond. Sci. Technol.* at press
[30] Turck B 1979 *J. Appl. Phys.* **50** 5397–401
[31] Turck B 1982 *Cryogenics* **22** 466–8
[32] Ito D, Koizumi M, Hamejima T and Nakane F 1983 *Cryogenics* **23** 643–8